Applied Energy 240 (2019) 709–718

Contents lists available at ScienceDirect

Applied Energy

journal homepage: www.elsevier.com/locate/apenergy

Modelling of a hybrid system for on-site power generation from solar fuels

Haoran Xu[a,b], Bin Chen[b], Peng Tan[c], Qiong Sun[d], M. Mercedes Maroto-Valer[a,*], Meng Ni[b,*]

[a] Research Centre for Carbon Solutions (RCCS), School of Engineering & Physical Sciences, Heriot-Watt University, Edinburgh EH14 4AS, United Kingdom
[b] Building Energy Research Group, Department of Building and Real Estate, The Hong Kong Polytechnic University, Hung Hom, Kowloon, Hong Kong, China
[c] Department of Thermal Science and Energy Engineering, University of Science and Technology of China, Hefei 230026, China
[d] School of Civil and Transportation Engineering, Guangdong University of Technology, Guangzhou 510006, China

HIGHLIGHTS

- The first 2D hybrid model combining photoreactor and SOFC is developed.
- A novel strategy towards power generation from solar energy is proposed.
- Zero CO_2 emission can be achieved during the operation of proposed system.
- Parametric studies are conducted with performance determining factors discussed.

ARTICLE INFO

Keywords:
Solid oxide fuel cell
Photoreactor
Solar energy
Hybrid system
Numerical simulation

ABSTRACT

Solar fuels, as clean and sustainable fuels, are promising energy sources for future low carbon economy. In this work, a hybrid system consisting of a photoreactor and a solid oxide fuel cell (SOFC) is proposed for on-site power generation from solar fuels. 2D numerical models are developed for the hybrid system for the first time by coupling the mass/momentum transport with the charge (electrons/ions) transport and the electrochemical/chemical reactions. A peak power density of 2162 $W\,m^{-2}$ is achieved from the SOFC at 1073 K operating temperature. However, a rapid drop of the power density is observed at large current density due to the fuel starvation in the anode. The inlet CO_2 mole fraction is found to significantly affect the output power density of the SOFC and CO_2 utilization rate of the photo reactor, where a CO_2 mole fraction of 40% is the optimum value for the studied cases. The results offer insightful information on energy conversion from solar to fuel to power and provide new options for sustainable energy conversion devices.

1. Introduction

Development of low-carbon and sustainable energy technologies has raised widely interest due to recent concerns about climate change and environmental problems [1–3]. Renewable energy technology such as photovoltaics (PV) is promising for sustainable energy utilization [4–6]. However, with the solar radiation being intermittent and unstable, a more effective energy storage and smarter transportation system is required for reliable energy supply [7–10]. Limited by complex energy storage and smart grid technologies, solar-driven fuel generation has become a viable solution towards solar energy harnessing and is worthy of significant effort [11–13].

In the process of solar fuel generation, solar energy is harvested by semiconductors, such as titanium dioxide (TiO_2) in a photoreactor [14–16]. On the catalyst surface, photochemical reduction reactions are initiated when electron–hole pairs are generated by light radiations [17]. Through photochemical reduction reactions, CO_2 and H_2O vapour can be reduced to CO, methane and other hydrocarbon fuels [18,19]. Since Fujishima & Honda first demonstrated the use of TiO_2 in photocatalytic H_2O splitting [20], the route from solar to fuel has been widely investigated by researchers all over the world. With the development of catalysts, higher light absorption, large surface area and improved charge separation were achieved by Kim et al. [21], where a methane generation rate of approximately 12 times higher than that of using pure TiO_2 was observed. Recently, Sorcar et al. [22] also described an efficient, stable, and readily synthesized CO_2-reduction photocatalyst, which produces a unprecedented high combined photocatalytic yield of ethane (2.7%) and methane (5.2%) over the 42 h test duration. In spite of significant progress in solar fuels synthesis, the direct utilization of product (the gas species mixture including hydrocarbons, CO, CO_2, H_2O, etc.) remains a problem [23].

Compared with the intermittent electrical power generation using

* Corresponding authors.
E-mail addresses: M.Maroto-Valer@hw.ac.uk (M.M. Maroto-Valer), bsmengni@polyu.edu.hk (M. Ni).

https://doi.org/10.1016/j.apenergy.2019.02.091
Received 25 November 2018; Received in revised form 13 February 2019; Accepted 17 February 2019

Nomenclature

Abbreviation

CFD	computational fluid dynamic
LSCF	lanthanum strontium cobalt ferrite
MSR	methane steam reforming
SCCM	standard cubic centimeters per minute
SDC	samaria-doped ceria
SOFC	solid oxide fuel cell
TiO_2	titanium dioxide
TPB	triple phase boundary
WGSR	water gas shift reaction
YSZ	yttrium stabilized zirconium

Roman

B_0	permeability coefficient, m^2
D_i^{eff}	effective diffusivity of species i, $m^2 \cdot s^{-1}$
D_{ik}^{eff}	Knudsen diffusion coefficient of i, $m^2 \cdot s^{-1}$
D_{im}^{eff}	molecular diffusion coefficient of i, $m^2 \cdot s^{-1}$
E_{act}	activation energy, $J \cdot mol^{-1}$
E_{CO}	equilibrium potential for carbon monoxide oxidization, V
E_{CO}^0	standard equilibrium potential for carbon monoxide oxidization, V
E_{eq}	equilibrium Nernst potential, V
E_{H_2}	equilibrium potential for hydrogen oxidization, V
$E_{H_2}^0$	standard equilibrium potential for hydrogen oxidization, V
F	Faraday constant, 96,485 $C \cdot mol^{-1}$
I	light intensity, $mW\,cm^{-2}$
i_o	exchange current density, $A \cdot m^{-2}$
k	rate constant of photochemical reduction
K_{H_2O}	ratio of rate constant for adsorption and desorption of H_2O
K_{CO_2}	ratio of rate constant for adsorption and desorption of CO_2
n	number of electrons transferred per electrochemical reaction
N_i	flux of mass transport, $kg \cdot m^{-3} \cdot s^{-1}$
p	(partial) pressure, Pa
R	gas constant, 8.314 $J \cdot mol^{-1} \cdot K^{-1}$
R_{MSR}	reaction rate of methane steam reforming, $mol \cdot m^{-3} \cdot s^{-1}$
R_{photo}	reaction rate of photochemical reduction, $mol \cdot m^{-3} \cdot s^{-1}$
R_{WGSR}	reaction rate of water gas shift reaction, $mol \cdot m^{-3} \cdot s^{-1}$
T	temperature, K
u	velocity field, $m^3 \cdot s^{-1}$
V	volume fraction
y_i	mole fraction of component i

Greek letters

α	charge transfer coefficient
β	reaction order of photochemical reduction
ε	porosity
η_{act}	activation polarization, V
η_{ohmic}	ohmic polarization, V
κ	permeability, m^2
μ	dynamic viscosity of fluid, Pa·s
ρ	fluid density, $kg \cdot m^{-3}$
σ	conductivity, S/m
γ	pre-exponential factor, $A\,m^{-2}$
τ	tortuosity
∅	potential, V

Subscripts

an	anode
ca	cathode
CO	carbon monoxide
CO_2	carbon dioxide
H_2	hydrogen
H_2O	steam
l	ionic phase
s	electronic phase

Superscripts

0	parameter at equilibrium conditions
eff	effective
L	local

solar cells, the utilization of solar fuels offers a potential way of continuous and stable power supply [24,25]. Therefore, the utilization of solar energy can be simplified by combining photochemical synthesis reactor with a device that can effectively utilize the mixture gas of solar fuel, such as solid oxide fuel cells (SOFCs).

SOFCs are electrochemical devices for converting chemical energy into electricity with high efficiency (> 60%) [26–28]. They are whole solid-state devices working quietly, usually with a dense ion-conducting electrolyte sandwiched between two electrodes [29,30]. Using this sandwich structure, fuel and oxidant (air) are well separated and the emission can be controlled in a way that the outlet gas can be recycled for an efficient loop [31,32]. Besides, the high operating temperature (about 800 °C) of SOFCs allows the use of non-noble catalyst (such as nickel) while keeping high electrochemical activity [33,34]. Fuel flexibility is another important advantage in SOFCs compared with low temperature fuel cells [35,36]. H_2, ammonia, various hydrocarbon fuels, and even solid carbon can be utilized for power generation [37–39]. In particular, the direct utilization of low-cost fuels (such as methane) in SOFCs has attracted great attention, where novel electrolyte structures have been proposed [40–42]. Due to the maturing market for SOFCs and their excellent scalability, SOFC-combined systems have been widely studied for further performance improvement [43–46].

It has been proved by previous researchers that SOFCs are very

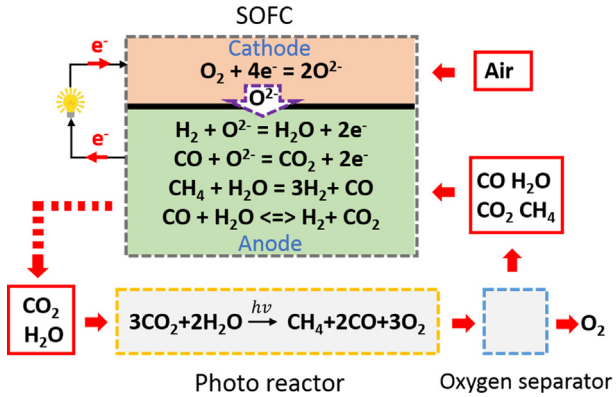

Fig. 1. Schematic of the hybrid system.

suitable components of hybrid systems; however, so far no work has been done to investigate a hybrid system combing a SOFC with a photoreactor to achieve on-site solar-fuel-to-power process (Fig. 1). Since this hybrid system has potential to realize low-carbon economy, it is of great importance to understand the detailed chemical/physical processes of the system. To fill the above-mentioned research gap, a hybrid system containing an SOFC and a photoreactor is proposed and

evaluated by a 2D mathematical model. The kinetics for the SOFC section are validated with the experimental data, whilst validated kinetics for the photoreactor section are adopted for model development. Parametric simulations are performed to gain insights in the coupled physical/chemical processes in the hybrid system for further optimization.

2. Model description

The proposed hybrid system mainly consists of a photoreactor and an SOFC, as shown in Fig. 1. The SOFC and the photoreactor are physically separated (which can be realized through multi-layer insulation structure), and their working temperatures are separately controlled. Thus, their different operating temperature will not affect each other. CO_2 and H_2O are introduced into the photoreactor, where they are reduced by solar energy to generate CH_4, CO and O_2. After O_2 separation, the mixed gas (containing CH_4, CO, CO_2 and H_2O) is supplied to the SOFC anode, where methane steam reforming (MSR) and water gas shift reaction (WGSR) take place and H_2 is generated through these reactions. In the anode, H_2 and CO are electrochemically oxidized to H_2O and CO_2 by the oxygen ions (O^{2-}), which is reduced from O_2 in the cathode and transported through the electrolyte. From the electrochemical oxidation reactions, the released electrons flow from the anode to cathode through the outer circuit and power is generated in this process.

In this study, 2D numerical models for the SOFC and the photoreactor are developed to simulate the characteristics of the hybrid system. Three sub-models are coupled, including SOFC sub-model, photoreactor sub-model and computational fluid dynamic (CFD) sub-model. For model simplification, the following assumptions are adopted:

1. The electrochemical reactions occur on the triple phase boundaries (TPBs), which are distributed uniformly in the porous electrodes.
2. The electronic and ionic conducting phases are continuous and homogeneous in the porous electrodes.
3. All the gases are considered as ideal gases.
4. Temperature distribution is uniform in the reactors due to the small size.
5. Only methane and CO are the fuels generated from photoreactor as described by Eq. (23).
6. The oxygen separator works perfectly and there is no species loss in the transportation.
7. Only H_2 and CO are electrochemically oxidized in the anode.
8. Light intensity for photoreactor is stable and constant.
9. Reaction order of the photocatalytic reaction is not affected by the light intensity.

2.1. SOFC chemical/electrochemical sub-model

Chemical and electrochemical reactions significantly affect the conversion of different species and the generation of electricity in the SOFC. Understanding this complicated process is a key step to the optimization of the hybrid system. Here, the SOFC sub-model is used to calculate the chemical and electrochemical reaction in the cell at given operating conditions such as applied voltage, operating temperature and inlet gas components. In accordance with the experiments for model validation [47], SOFC has the thickness of its anode, electrolyte and cathode being 400 μm, 8 μm and 24 μm, respectively. The cell is made of Ni-yttrium stabilized zirconium (YSZ) composite anode, YSZ/samaria-doped ceria (SDC) bilayer electrolyte and lanthanum strontium cobalt ferrite (LSCF) cathode. The properties of these materials including their conductivities, porosities and volume fractions can be found in Table 1.

2.1.1. Chemical reactions in the SOFC

The mixture of CH_4, H_2O, CO and CO_2 is supplied to the anode and air is supplied to the cathode (Fig. 1). In the porous anode, MSR and WGSR happen, as shown in Eqs. (1) and (2)

$$CH_4 + H_2O = CO + 3H_2 \quad (1)$$

$$CO + H_2O = CO_2 + H_2 \quad (2)$$

For the calculation of MSR rate (R_{MSR} mol m^{-3} s^{-1}) and WGSR rate (R_{WGSR} mol m^{-3} s^{-1}), the following widely validated expressions are adopted [48]:

$$R_{MSR} = k_{rf}\left(p_{CH_4}p_{H_2O} - \frac{p_{H_2}^3 p_{CO}}{K_{pr}}\right) \quad (3)$$

$$k_{rf} = 2395\exp\left(\frac{-231266}{RT}\right)(\text{mol m}^{-3}\ \text{Pa}^{-2}\ \text{s}^{-1}) \quad (4)$$

$$K_{pr} = 1.0267 \times 10^{10}\exp(-0.2513Z^4 + 0.3665Z^3 + 0.5810Z^2 - 27.134Z + 3.277) \quad (5)$$

$$Z = \frac{1000}{T} - 1 \quad (6)$$

$$R_{WGSR} = k_{sf}\left(p_{H_2O}p_{CO} - \frac{p_{H_2}p_{CO_2}}{K_{ps}}\right) \quad (7)$$

$$k_{sf} = 0.0171\exp\left(\frac{-103191}{RT}\right)(\text{mol m}^{-3}\ \text{Pa}^{-2}\ \text{s}^{-1}) \quad (8)$$

$$K_{ps} = \exp(-0.2935Z^3 + 0.6351Z^2 + 4.1788Z + 0.3169) \quad (9)$$

2.1.2. Electrochemical reactions

In the cathode, O^{2-} ions are generated through the electrochemical

Table 1
Kinetic parameters for SOFC section.

Parameters	Value or expression	Unit
Ionic conductivity		
YSZ	$3.34 \times 10^4 e^{\frac{-10300}{T}}$	Sm^{-1}
SDC	$\frac{100}{T} \times 10^{5.48077-\frac{3792.53}{T}}$	Sm^{-1}
LSCF	$\frac{100}{T} \times 10^{2.51289-\frac{3036.75}{T}}$	Sm^{-1}
Electronic conductivity		
LSCF	$\frac{100}{T} \times 10^{4.32576+\frac{1204.26}{T}}$	Sm^{-1}
Ni	$3.27 \times 10^6 - 1065.3T$	Sm^{-1}
Porosity		
Cathode	0.2	
Anode	0.6	
Anode volume fraction		
YSZ	0.4	
Ni	0.6	
Area of TPB		
Cathode layer	2.14×10^5	m^2 m^{-3}
Anode layer	2.14×10^5	m^2 m^{-3}
Electrode tortuosity		
Anode	3	
Cathode	3	
Electrochemical reaction		
i_{H_2}	5300	A m^{-2}
i_{CO}	2410	A m^{-2}
i_{O_2}	5010	A m^{-2}
α_{H_2}	0.5	
α_{CO}	0.5	
α_{O_2}	0.85	

Table 2
Validated kinetic parameters for photo reduction reaction.

Parameter	Value	Unit
k	5000	μmole g catal.$^{-1}$
I	150	mW cm^{-2}
β	0.60	
K_{H_2O}	0.75	bar^{-1}
K_{CO_2}	30	bar^{-1}

Table 3
Operating parameters for SOFC temperature effects study.

Parameter	Value	Unit
Photoreactor inlet gas flow rate	100	SCCM
Photoreactor inlet gas composition	CO_2 (40%), H_2O (60%)	
SOFC cathode gas flow rate	100	SCCM
SOFC cathode gas composition	Air	
SOFC operating temperature	973–1173	K
SOFC operating voltage	0.7	V

Table 4
Operating parameters for SOFC applied voltage effects study.

Parameter	Value	Unit
Photoreactor inlet gas flow rate	100	SCCM
Photoreactor inlet gas composition	CO_2 (40%), H_2O (60%)	
SOFC cathode gas flow rate	100	SCCM
SOFC cathode gas composition	Air	
SOFC operating temperature	973, 1073	K
SOFC operating voltage	0.2–0.7	V

Table 5
Operating parameters for photoreactor inlet gas composition effect study.

Parameter	Value	Unit
Photoreactor inlet gas flow rate	100	SCCM
Photoreactor inlet gas composition	CO_2 (10–90%), H_2O (100% - CO_2)	
SOFC cathode gas flow rate	100	SCCM
SOFC cathode gas composition	Air	
SOFC operating temperature	1073	K
SOFC operating voltage	0.7	V

Table 6
Operating parameters for light intensity effect study.

Parameter	Value	Unit
Photoreactor inlet gas flow rate	200	SCCM
Photoreactor inlet gas composition	CO_2 (40%), H_2O (60%)	
SOFC cathode gas flow rate	100	SCCM
SOFC cathode gas composition	Air	
SOFC operating temperature	1073	K
SOFC operating voltage	0.7	V
Light intensity	150–300	mW cm^{-2}

reduction of O, as shown in Eq. (10):

$$O_2 + 4e^- = 2O^{2-} \quad (10)$$

In the anode, H_2 and CO are electrochemically oxidized by the O^{2-} ions transported from the cathode and electrons are released in this process as shown in Eqs. (11) and (12):

$$H_2 + O^{2-} = H_2O + 2e^-. \quad (11)$$

$$CO + O^{2-} = CO_2 + 2e^-. \quad (12)$$

During operation, the output voltage from the SOFC can be calculated by extracting activation overpotential (η_{act}) and ohmic overpotential (η_{ohmic}) from the equilibrium overpotential (E_{eq}) as shown in Eq. (13):

$$V = E_{eq} - \eta_{act} - \eta_{ohmic}, \quad (13)$$

It should be noted that the equilibrium overpotential is calculated based on local gas partial pressures, so that concentration overpotential is included.

2.1.2.1. Equilibrium potential. Equilibrium potential is related with thermodynamic. The calculation of equilibrium potentials for H_2 and CO electrochemical oxidization can be expressed by Eqs. (14) and (15):

$$E_{H_2} = E^0_{H_2} + \frac{RT}{2F}\ln\left[\frac{P^L_{H_2}(P^L_{O_2})^{1/2}}{P^L_{H_2O}}\right] \quad (14)$$

$$E_{CO} = E^0_{CO} + \frac{RT}{2F}\ln\left[\frac{P^L_{CO}(P^L_{O_2})^{1/2}}{P^L_{CO_2}}\right] \quad (15)$$

Here $P^L_{H_2O}$, $P^L_{H_2}$, $P^L_{CO_2}$, P^L_{CO} and $P^L_{O_2}$are local partial pressures of H_2O, H_2, CO_2, CO and O_2, respectively. R is the gas constant (8.3145 J mol^{-1} K^{-1}), F is the Faraday constant (96,485 C mol^{-1}), T is the working temperature (K), and E^0_{CO} and $E^0_{H_2}$ are standard potentials, which can be calculated by Eqs. (16) and (17):

$$E^0_{H_2} = 1.253 - 0.00024516T \ (V) \quad (16)$$

$$E^0_{CO} = 1.46713 - 0.0004527T \ (V) \quad (17)$$

2.1.2.2. Activation potential. Activation overpotential reflects the activity of the electrochemical reactions. It is related with the property of reactants and catalytic material. The Butler-Volmer equation is employed to calculate the activation overpotential (η_{act}), as shown in Eq. (18).

$$i = i_0\left\{\exp\left(\frac{\alpha n F \eta_{act}}{RT}\right) - \exp\left(-\frac{(1-\alpha)nF\eta_{act}}{RT}\right)\right\}, \quad (18)$$

Here, i_0 is the exchange current density (Am^{-2}) and α is the transfer coefficient. These two parameters are tuning parameters in fitting the simulation results with experimental data. As both H_2 and CO can be electrochemically oxidized in the anode, the exchange current density of H_2 is set to be 2.2 times of CO according to previous study [49].

2.1.2.3. Ohmic potential. The ohmic overpotential (η_{ohmic}) can be calculated by the Ohm's law, as shown in Eqs. (19) and (20).

$$i_l = -\sigma_l^{eff}\nabla(\varnothing_l) \quad (19)$$

$$i_s = -\sigma_s^{eff}\nabla(\varnothing_s) \quad (20)$$

Here, $\varnothing_l$ and $\varnothing_s$are the ionic and electronic potentials, respectively. In the typical composite electrodes, the effective conductivities (σ_l^{eff} and σ_s^{eff}) can be further expressed as Eqs. (21) and (22), respectively.

$$\sigma_l^{eff} = \sigma_l \cdot \frac{V_l}{\tau_l} \quad (21)$$

$$\sigma_s^{eff} = \sigma_s \cdot \frac{V_s}{\tau_s} \quad (22)$$

Here, σ is the intrinsic conductivity, V is the volume fraction value and τ is the tortuosity value. Related parameter values of SOFC submodel can be found in Table 1.

2.2. Photoreactor reaction sub-model

The photoreactor model contains photochemical reaction and computational fluid dynamic (CFD) for the calculation of species

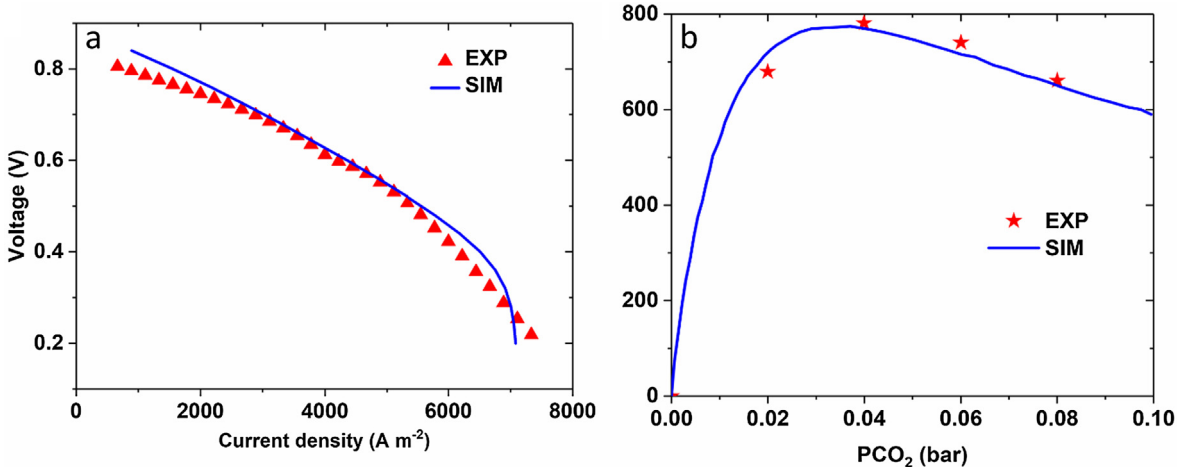

Fig. 2. Model validation for (a) SOFC chemical/electrochemical sub-model and (b) photoreactor reaction sub-model.

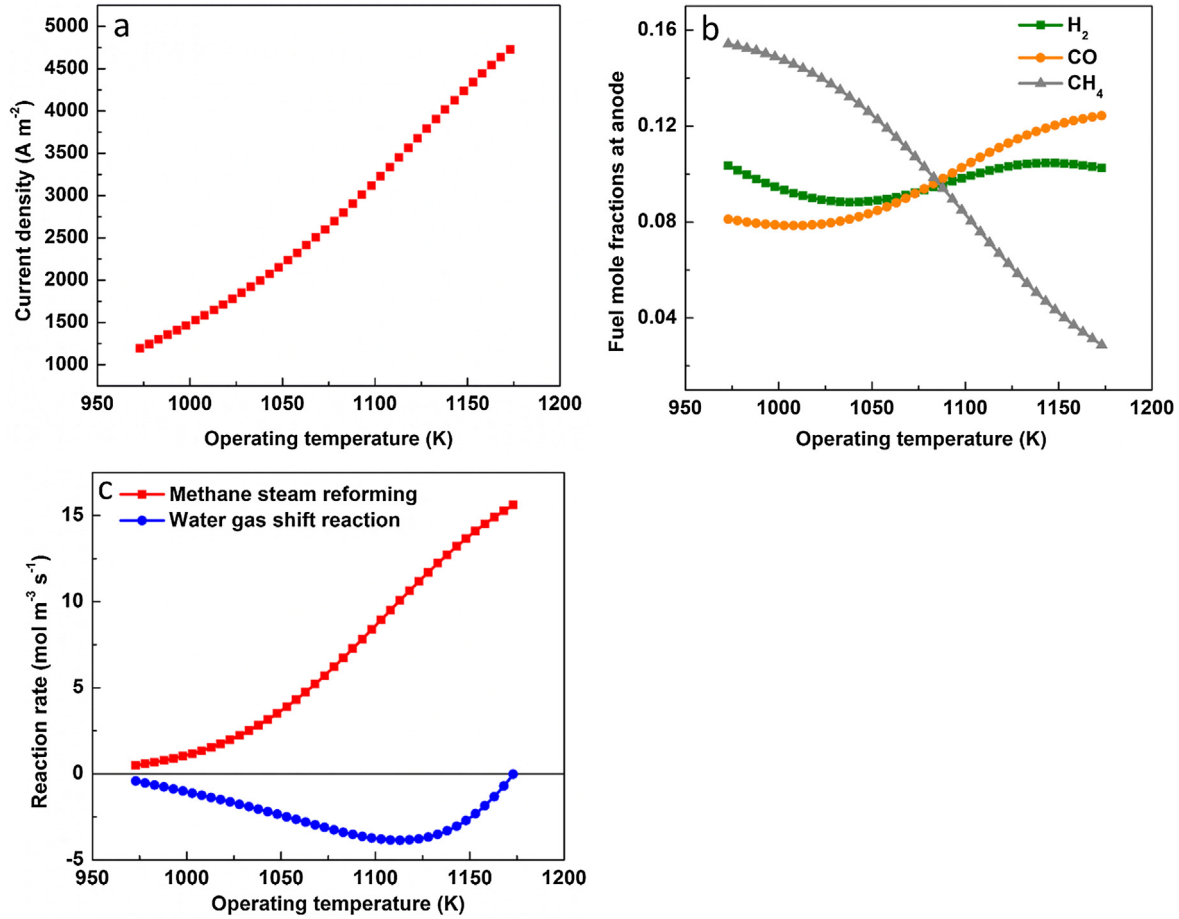

Fig. 3. The effects of SOFC operating temperature on (a) the output current density, (b) the mole fractions of fuel at anode and (c) the MSR and WGSR rates.

generation/consumption rate and distribution in the calculation domain.

Fuels for the SOFC are generated by the photoreactor through photochemical reductions of CO_2 and H_2O. In accordance with the experiments conducted by Tahir et al. [50], a montmorillonite (MMT)/TiO2 coated monolith photoreactor is adopted. The photochemical reaction rate directly affects the concentration of solar fuels and the subsequent power generation in the SOFC. Therefore, it is important to study the effects of given operating conditions on the photoreactor such as the inlet gas component and light intensity. Here, the photoreactor reaction sub-model is used to calculate the photo reduction reaction rates (R_{photo} mol $m^{-3} s^{-1}$) of CO_2 and H_2O at given operating parameters. The kinetic model is based on the experimental results and numerically validated from Tahir et al. [50] as follows:

$$3CO_2 + 2H_2O \rightarrow CH_4 + 2CO + 3O_2 \quad (23)$$

$$R_{photo} = kI^{\alpha}\left(\frac{K_{H_2O}P^{L}_{H_2O}K_{CO_2}P^{L}_{CO_2}}{(1 + K_{H_2O}P^{L}_{H_2O} + K_{CO_2}P^{L}_{CO_2})^2}\right) \quad (24)$$

Here, k is the rate constant, I is light intensity and α is reaction

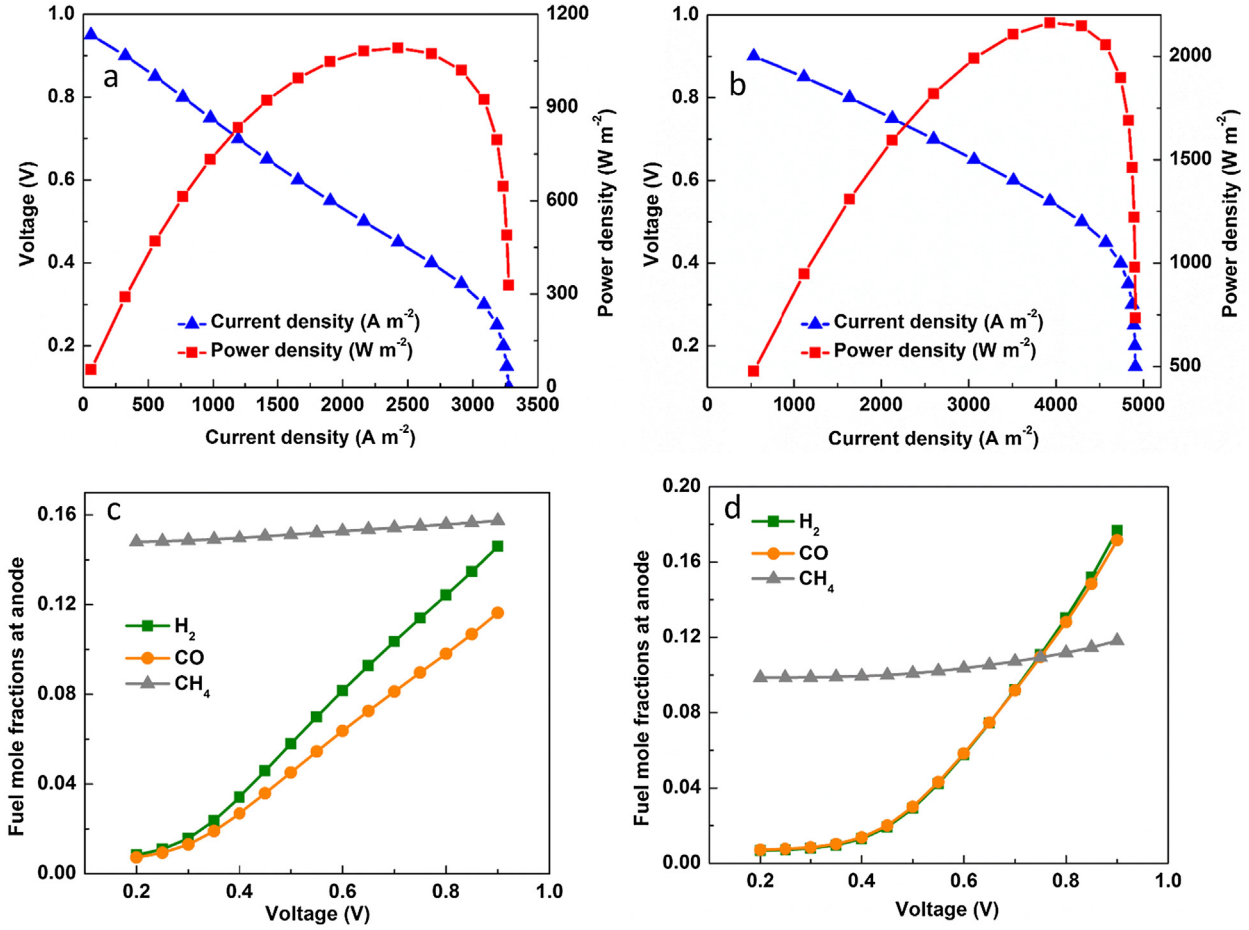

Fig. 4. The effects of applied voltage on the output power and mole fractions of fuel at anode at 973 K and 1073 K operating temperature.

order. K_{H_2O} and K_{CO_2} are the constants for adsorption and desorption of H_2O and CO_2, respectively. Related kinetic parameters are listed in Table 2.

2.3. Computational fluid dynamic (CFD) sub-model

The mass transport and momentum transport are important physical processes that affect the species distribution in both the photoreactor and SOFC. The CFD model is also coupled with the chemical/electrochemical model, thus affects the chemical electrochemical reactions rate in the SOFC and photoreactor. With the solar-fuels transporting from photoreactor to the SOFC in the hybrid system, the CFD sub-model connects the SOFC chemical/electrochemical sub-model and photoreactor reaction sub-model. In the CFD sub-model, mass transport of gas species is calculated by extended Fick's law as shown in Eq. (25).

$$N_i = -\frac{1}{RT}\left(\frac{B_0 y_i P}{\mu}\nabla P - D_i^{eff}\nabla(y_i P)\right) \quad (i = 1,\ldots,n), \tag{25}$$

Here, B_0 is the permeability, μ is the gas viscosity, y_i and D_i^{eff} are the mole fraction and effective diffusivity of component i, respectively. D_i^{eff} can be further determined by Eq. (26).

$$D_i^{eff} = \frac{\varepsilon}{\tau}\left(\frac{1}{D_{im}^{eff}} + \frac{1}{D_{ik}^{eff}}\right)^{-1}, \tag{26}$$

Here, ε is the porosity, τ is the tortuosity factor, D_{im}^{eff} is the molecular diffusion coefficient and D_{ik}^{eff} is the Knudsen diffusion coefficient [51].

When coupled with chemical/electrochemical reactions, the mass conservation can be calculated by Eq. (27).

$$\nabla(-D_i^{eff}\nabla c_i) = r_i, \tag{27}$$

Here, c_i is the gas molar concentration and r_i is the mass source term of the gaseous species.

The momentum transport is calculated by Navier-Stokes equation with Darcy's term as shown in Eq. (28).

$$\rho\frac{\partial u}{\partial t} + \rho u\nabla u = -\nabla p + \nabla[\mu(\nabla u + (\nabla u)^T) - \frac{2}{3}\mu\nabla u] - \frac{\varepsilon\mu u}{k} \tag{28}$$

Here, ρ is the gas density and u is the velocity vector.

2.4. Boundary conditions

The electric potentials are specified at the outer boundaries of anode and cathode, respectively. Insulation condition is specified at the bottom and top of the SOFC. Inlet gas flow rate and mole fraction of the species are given at inlets of the photoreactor. The inlet gas of SOFC anode is the same with the outlet of photoreactor, while O_2 is excluded. Pressure conditions are specified for both SOFC and photoreactor, respectively. Specific boundary condition values can be found in Tables 2–6 for each parametric study. The numerical models are solved at given parameters using commercial software COMSOL MULTIPHYSICS®.

2.5. Model validation

In the SOFC sub-model, the same material and geometry are adopted in accordance with the experiments conducted by Xu et al. [47]. The kinetic parameters of the solid oxide cell are validated by comparing the current-voltage characteristic of simulation results and

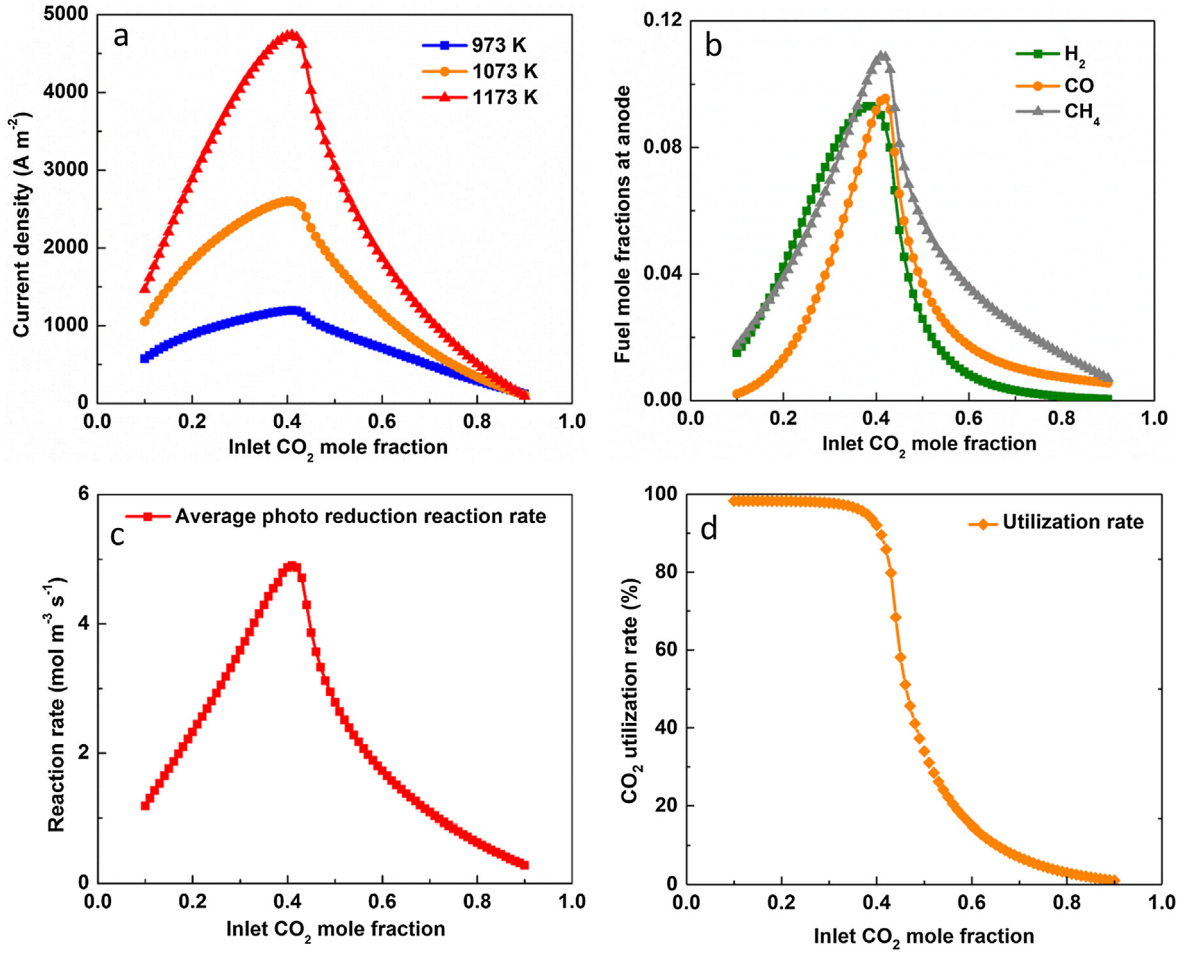

Fig. 5. The effects of inlet CO_2 mole fraction on (a) output current density, (b) mole fractions of fuel at anode, (c) average photo reduction reaction rate and (d) CO_2 utilization rate.

experimental data with good agreement, as shown in Fig. 2a. In the subsequent parametric study, the same cell structure and tuning parameters are used and the cell area is extended to 1 cm × 10 cm for the study of practical application.

In the photoreactor sub-model, the same operating temperature and pressure are used in accordance with the experiments. The experimental and simulation data of methane yield rate at different CO_2 partial pressures are compared for model validation. According to the testing and simulation results reported by Tahir et al. [50] (as shown in Fig. 2b), the validated Langmuir-Hinshelwood kinetic model is adopted. In the parametric study, the reaction area of photoreactor is set to be 10 cm × 10 m with a thickness of 2 μm to match the reaction rates of the SOFC.

3. Results and discussion

To investigate the effects of operating conditions on the system performance, parametric studies are conducted by varying the operating temperature, applied voltage and inlet CO_2 mole fraction. For the performance evaluation, CO_2 utilization rate is the main evaluation criterion in the photoreactor, while the output power density and CO_2 recovery rate are the main criteria in the SOFC section.

3.1. Effect of SOFC operating temperature

The operating temperature is a key parameter affecting the chemical and electrochemical kinetics in the SOFC. In this parametric study, the operating temperature is varied from 973 K to 1173 K, while other operating conditions are kept as constant, as shown in Table 3.

As found in Fig. 3a, the output current density at given applied voltage is significantly affected by the operating temperature. With the operating temperature increasing from 973 K to 1173 K, the output current density raises quickly from 1194 A m^{-2} to 4728 A m^{-2}, which shows a more than 3 times improvement. Meanwhile, there is no significant decrease of H_2 or CO mole fractions observed at anode with the increase of operating temperature, as shown in Fig. 3b. Although the high operating temperature results in a faster electrochemical consumption of H_2 and CO, the consumed H_2 and CO are recovered by the largely improved MSR rate at high operating temperature. As can be seen form Fig. 3c, the MSR rate increases from 0.5 mol m^{-3} s^{-1} at 973 K to 15.6 mol m^{-3} s^{-1} at 1173 K. The quick MSR rate also explains the significant decrease of CH_4 mole fraction at high temperature, as shown in Fig. 3b. Compared with the steady growth of MSR rate with the increase of operating temperature, the WGSR rate keeps negative and reaches a peak at 1113 K, which means H_2 and CO_2 are consumed to generate CO and H_2O for the balance of gas species.

3.2. Effect of applied voltage

As the main product from the proposed system, output power is significantly affected not only by the operating temperature, but also by the applied voltage. In this parametric study, the applied voltage is varied from 0.2 V to 0.9 V at 973 K and 1073 K operating temperature, respectively. The other operating parameters are kept constant as shown in Table 4.

At both two operating temperatures, the current densities enjoy a

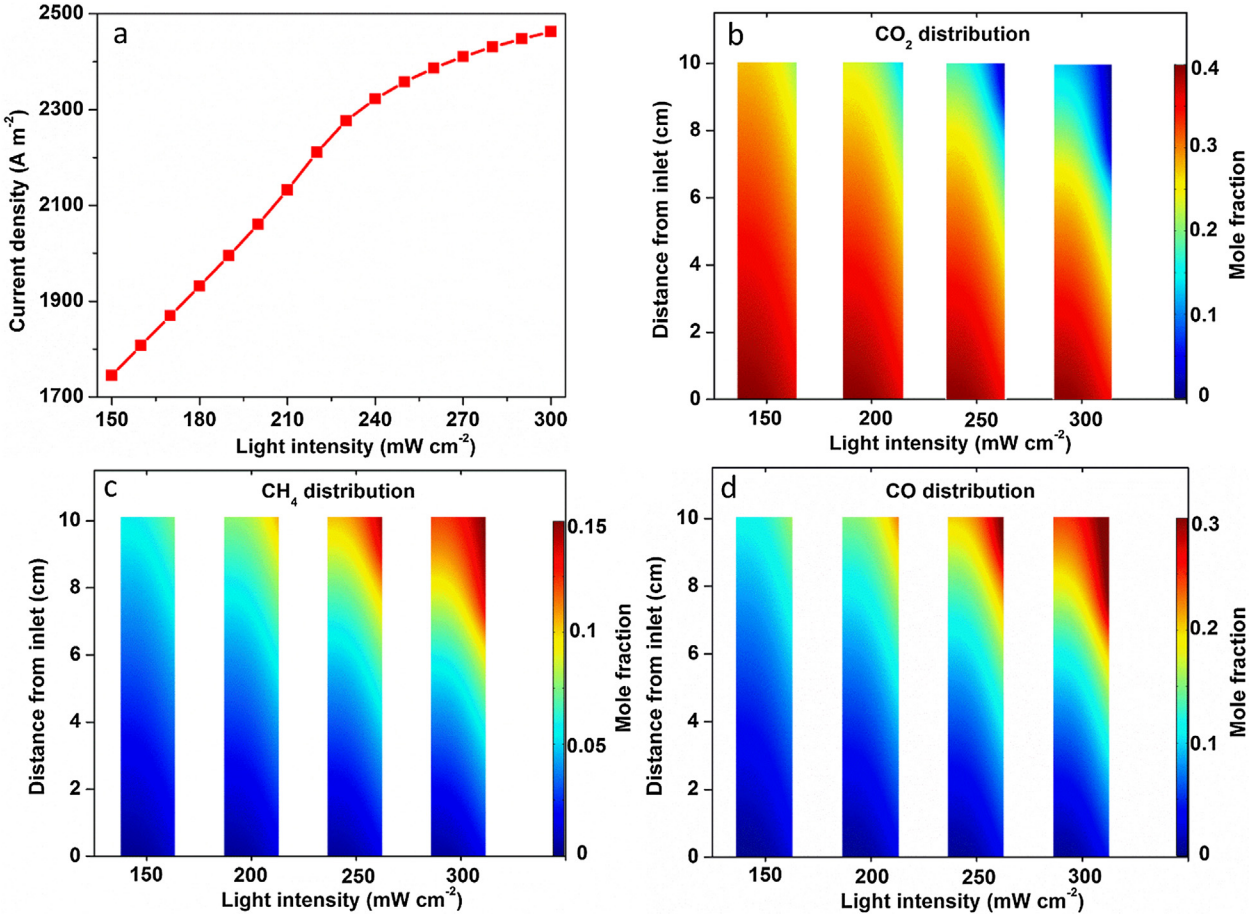

Fig. 6. The effects of light intensity on (a) output current density, (b) CO_2 mole fraction distribution, (c) CH_4 mole fraction distribution and (d) CO mole fraction distribution in the photoreactor.

quick increase while reach a limitation at ~3200 A m^{-2} (973 K) and 5000 A m^{-2} (1073 K) as shown in Fig. 4a and b, respectively. In accordance with this, their power densities boost in the beginning and fall off quickly form the peak power density of 1092 W m^{-2} (973 K) and 2162 W m^{-2} (1073 K), respectively. This significant decline is mainly caused by fuel starvation, as can be found in Fig. 4c and d. With the decrease of applied voltage, a higher activation overpotential can be applied to the electrochemical reaction, which significantly increases the electrochemical reaction rate. Therefore, H_2 and CO are quickly consumed, and their mole fractions are significantly declined. When the cell works at 0.2 V applied voltage and 1073 K operating temperature, only 0.67% of H_2 and 0.71% of CO exist in the anode. It can also be found that the mole faction of CH_4 is much higher than H_2 and CO at low voltage, indicating a faster MSR rate can be helpful to ease the fuel-starvation phenomenon.

3.3. Effect of inlet CO_2 mole fraction

The mole fraction of inlet gas specie is an important parameter that affects both the photo reduction rate and gas utilization. In this parametric study, the inlet CO_2 mole fraction is varied from 0.1 to 0.9 at given SOFC operating temperatures, while other operating conditions are kept as constant, as shown in Table 5.

As shown in Fig. 5a, the current density is significantly affected by the inlet CO_2 mole fraction at all three given temperatures. In accordance with previous analysis in Section 3.1, the highest SOFC operating temperature (1173 K) provides the largest peak current density (4736 A m^{-2}) and the lowest operating temperature (973 K) provides the smallest peak current density (1196 A m^{-2}). However, along with the increase of inlet CO_2 mole fraction, the current densities rise in the beginning and decrease continuously until reach a very low value (about 100 A m^{-2}) when the inlet CO_2 mole fraction is increased to 0.9. This huge difference can be explained by the similar tendency of mole fraction changes of the fuels at anode as shown in Fig. 5b. The mole fractions of H_2, CO and CH_4 at anode all reach peak values, when the inlet CO_2 mole fraction is controlled at ~0.4. The further explanation comes from the effects of inlet CO_2 mole fraction on the photo reduction rate, as shown in Fig. 5c, which also shows a peak photo reduction reaction rate at ~0.4 inlet CO_2 mole fraction, while the rate quickly decreases with the further increase of inlet CO_2 mole fraction. In addition, a high inlet CO_2 mole fraction not only lowers down the current density, but also reduces the CO_2 utilization rate. As shown in Fig. 5d, the CO_2 utilization rate is close to 100% when the inlet CO_2 mole fraction is less than 0.4. However, it quickly decreases to less than 10% when the inlet CO_2 mole fraction is high than 0.66.

3.4. Effect of light intensity

Light intensity is an important factor that affects the photochemical reaction rate. In this parametric study, the light intensity is varied from 150 to 300 mW cm^{-2} (which is stronger than the light intensity given in Ref. [50]), while other operating conditions are kept constant, as shown in Table 6.

As shown in Fig. 6a, the current density is promoted from 1745 to 2462 A m^{-2} with the light intensity increasing from 150 to 300 mW cm^{-2}. Since the applied voltage is kept at 0.7 V, the increase of output current density also means the increase of output power density with the increase of light intensity. This significant improvement is

mainly contributed by the improved CO_2 conversion rate as well as the solar-fuel concentration in the photoreactor as shown in Fig. 6b–d. With the increase of light intensity from 150 to 200, 250 and 300 mW cm^{-2}, the mole fraction of CO_2 continuously decreases from 0.25 to 0.19, 0.12 and 0.08 at the outlet of the photoreactor, respectively. Meanwhile, the mole factions of CH_4 and CO continuously increases from 0.07 to 0.09, 0.12 and 0.13 and from 0.13 to 0.18, 0.25 and 0.28 at the outlet of the photoreactor, respectively. Therefore, a stronger light intensity is very helpful to improve the performance of the hybrid system, which can be achieved by concentrating the sunlight to the photoreactor.

4. Conclusions

In summary, a novel strategy towards power generation from solar energy has been put forward in this work. With the reduction of CO_2 with H_2O in the photoreactor, the outlet gas mixture can be directly utilized in the SOFC after O_2 separation. 2D numerical models are developed to investigate the detailed chemical/physical process in the hybrid system and parametric studies are conducted for performance optimization. The kinetics of SOFC sub-model and photoreactor sub-model are validated by comparing experimental data with simulation results, where there are only 5% and 3% relative errors for each sub-model, respectively.

Through numerical simulation, we observed that the opetating temperature of the SOFC, the applied voltage and the inlet gas component of the photoreactor have great influence on the output power density. In addition, the reaction rate of MSR plays an important role to prevent the fuel starvation in the electrochemical reactions of the SOFC. Considering the relative lower fuel concentration, a relative higher operating voltage is suggested. Adding an external fuel inlet for the SOFC anode can also help release the “fuel-starvation” problem, while its detailed effects on the overall system performance needs future study. A peak power density of 2162 W m^{-2} is obtained at 1073 K operating temperature of the SOFC. The stronger light intensity is also found to significantly improve the output current density and CO_2 conversion rate, thus concentrating the sunlight to the photoreactor is also suggested.

Although the preliminary results are promising, challenges need to be carefully addressed such as the low solar-to fuel efficiency (< 1%), low photochemical reduction rate, effective O_2 separation and fuel storage. More studies are needed to improve this hybrid system. For example, the development of an effective separator membrane, highly active photocatalyst, direct utilization of separated oxygen and advanced recycle design are needed. Overall, this photoreactor-SOFC hybrid system demonstrates a new design with promising preliminary performance for power generation from solar energy and build a solid foundation to undestand the chemical/physical mechanism of the system, and more importantly, offers a feasible and effective approach for achieving stable solar-to-power energy devices.

Acknowledgements

This research is supported by a grant (Project Number: PolyU 152214/17E) from Research Grant Council, University Grants Committee, Hong Kong SAR, as well as financial support provided by the UK Engineering and Physical Sciences Research Council (EP/K021796/1 and EP/N009924/1) and the Research Centre for Carbon Solutions (RCCS) at Heriot–Watt University. The authors would also like to thank Ms. Zhen YAO at the University of St Andrews for language polishing.

References

[1] Santer BD, Wehner MF, Wigley TML, Sausen R, Meehl GA, Taylor KE, et al. Contributions of anthropogenic and natural forcing to recent tropopause height changes. Science 2003;301(5632):479–83.
[2] Cinti G, Baldinelli A, Di Michele A, Desideri U. Integration of solid oxide electrolyzer and Fischer-Tropsch: a sustainable pathway for synthetic fuel. Appl Energy 2016;162:308–20.
[3] Lahijani P, Zainal ZA, Mohammadi M, Mohamed AR. Conversion of the greenhouse gas CO2 to the fuel gas CO via the Boudouard reaction: A review. Renew Sustain Energy Rev 2015;41:615–32.
[4] Eriksson ELV, Gray EM. Optimization and integration of hybrid renewable energy hydrogen fuel cell energy systems – A critical review. Appl Energy 2017;202:348–64.
[5] Mazzio KA, Luscombe CK. The future of organic photovoltaics. Chem Soc Rev 2015;44(1):78–90.
[6] Schuergers N, Werlang C, Ajo-Franklin CM, Boghossian AA. A synthetic biology approach to engineering living photovoltaics. Energy Environ Sci 2017;10(5):1102–15.
[7] Kucharski TJ, Tian Y, Akbulatov S, Boulatov R. Chemical solutions for the closed-cycle storage of solar energy. Energy Environ Sci 2011;4(11):4449–72.
[8] Weldekidan H, Strezov V, Town G. Review of solar energy for biofuel extraction. Renew Sustain Energy Rev 2018;88:184–92.
[9] Xu H, Chen B, Ni M. Modeling of direct carbon-assisted solid oxide electrolysis cell (SOEC) for syngas production at two different electrodes. J Electrochem Soc 2016;163(11):F3029–35.
[10] Köktürk G, Tokuç A. Vision for wind energy with a smart grid in Izmir. Renew Sustain Energy Rev 2017;73:332–45.
[11] Kwak BS, Chae J, Kang M. Design of a photochemical water electrolysis system based on a W-typed dye-sensitized serial solar module for high hydrogen production. Appl Energy 2014;125:189–96.
[12] Kuramochi Y, Ishitani O, Ishida H. Reaction mechanisms of catalytic photochemical CO_2 reduction using Re(I) and Ru(II) complexes. Coord Chem Rev 2017.
[13] Young KJ, Martini LA, Milot RL, Snoeberger RC, Batista VS, Schmuttenmaer CA, et al. Light-driven water oxidation for solar fuels. Coord Chem Rev 2012;256(21):2503–20.
[14] Dhakshinamoorthy A, Navalon S, Corma A, Garcia H. Photocatalytic CO_2 reduction by TiO_2 and related titanium containing solids. Energy Environ Sci 2012;5(11):9217–33.
[15] El-Maghrabi HH, Barhoum A, Nada AA, Moustafa YM, Seliman SM, Youssef AM, et al. Synthesis of mesoporous core-shell CdS@TiO_2 (0D and 1D) photocatalysts for solar-driven hydrogen fuel production. J Photochem Photobiol, A 2018;351:261–70.
[16] Ola O, Maroto-Valer MM. Review of material design and reactor engineering on TiO_2 photocatalysis for CO_2 reduction. J Photochem Photobiol, C 2015;24:16–42.
[17] Delavari S, Amin NAS. Photocatalytic conversion of CO_2 and CH_4 over immobilized titania nanoparticles coated on mesh: Optimization and kinetic study. Appl Energy 2016;162:1171–85.
[18] Roy SC, Varghese OK, Paulose M, Grimes CA. Toward solar fuels: photocatalytic conversion of carbon dioxide to hydrocarbons. ACS Nano 2010;4(3):1259–78.
[19] Kalamaras E, Maroto-Valer MM, Shao M, Xuan J, Wang H. Solar carbon fuel via photoelectrochemistry. Catal Today 2018.
[20] Fujishima A, Honda K. Electrochemical photolysis of water at a semiconductor electrode. Nature 1972;238:37.
[21] Kim K, Razzaq A, Sorcar S, Park Y, Grimes CA, In S-I. Hybrid mesoporous Cu_2ZnSnS_4 (CZTS)–TiO_2 photocatalyst for efficient photocatalytic conversion of CO_2 into CH_4 under solar irradiation. RSC Adv 2016;6(45):38964–71.
[22] Sorcar S, Thompson J, Hwang Y, Park YH, Majima T, Grimes CA, et al. High-rate solar-light photoconversion of CO_2 to fuel: controllable transformation from C1 to C2 products. Energy Environ Sci 2018.
[23] Herron JA, Kim J, Upadhye AA, Huber GW, Maravelias CT. A general framework for the assessment of solar fuel technologies. Energy Environ Sci 2015;8(1):126–57.
[24] Styring S. Artificial photosynthesis for solar fuels. Faraday Discuss 2012;155:357–76.
[25] Lewis NS. Research opportunities to advance solar energy utilization. Science 2016;351(6271).
[26] Gür TM. Comprehensive review of methane conversion in solid oxide fuel cells: Prospects for efficient electricity generation from natural gas. Prog Energy Combust Sci 2016;54:1–64.
[27] Sharma M, Rakesh N, Dasappa S. Solid oxide fuel cell operating with biomass derived producer gas: Status and challenges. Renew Sustain Energy Rev 2016;60:450–63.
[28] Park S, Vohs JM, Gorte RJ. Direct oxidation of hydrocarbons in a solid-oxide fuel cell. Nature 2000;404(6775):265–7.
[29] Minh NQ. Solid oxide fuel cell technology—features and applications. Solid State Ionics 2004;174(1):271–7.
[30] Mahato N, Banerjee A, Gupta A, Omar S, Balani K. Progress in material selection for solid oxide fuel cell technology: A review. Prog Mater Sci 2015;72:141–337.
[31] Ormerod RM. Solid oxide fuel cells. Chem Soc Rev 2003;32(1):17–28.
[32] Jiang C, Ma J, Bonaccorso AD, Irvine JTS. Demonstration of high power, direct conversion of waste-derived carbon in a hybrid direct carbon fuel cell. Energy Environ Sci 2012;5(5):6973–80.
[33] Shi Y, Cai N, Mao Z. Simulation of EIS spectra and polarization curves based on Ni/YSZ patterned anode elementary reaction models. Int J Hydrogen Energy 2012;37(1):1037–43.
[34] Cheng Z, Wang J-H, Choi Y, Yang L, Lin MC, Liu M. From Ni-YSZ to sulfur-tolerant anode materials for SOFCs: electrochemical behavior, in situ characterization, modeling, and future perspectives. Energy Environ Sci 2011;4(11):4380–409.
[35] Rady AC, Giddey S, Badwal SPS, Ladewig BP, Bhattacharya S. Review of fuels for direct carbon fuel cells. Energy Fuels 2012;26(3):1471–88.
[36] Antunes R, Skrzypkiewicz M. Chronoamperometric investigations of electro-

oxidation of lignite in direct carbon bed solid oxide fuel cell. Int J Hydrogen Energy 2015;40(12):4357–69.
[37] Xu H, Chen B, Liu J, Ni M. Modeling of direct carbon solid oxide fuel cell for CO and electricity cogeneration. Appl Energy 2016;178:353–62.
[38] Ni M. Modeling and parametric simulations of solid oxide fuel cells with methane carbon dioxide reforming. Energy Convers Manage 2013;70:116–29.
[39] Giddey S, Badwal SPS, Kulkarni A, Munnings C. A comprehensive review of direct carbon fuel cell technology. Prog Energy Combust Sci 2012;38(3):360–99.
[40] Guo Y, Bessaa M, Aguado S, Steil MC, Rembelski D, Rieu M, et al. An all porous solid oxide fuel cell (SOFC): a bridging technology between dual and single chamber SOFCs. Energy Environ Sci 2013;6(7):2119–23.
[41] Xu H, Chen B, Tan P, Cai W, He W, Farrusseng D, et al. Modeling of all porous solid oxide fuel cells. Appl Energy 2018;219:105–13.
[42] Xu H, Chen B, Tan P, Xuan J, Maroto-Valer MM, Farrusseng D, et al. Modeling of all-porous solid oxide fuel cells with a focus on the electrolyte porosity design. Appl Energy 2019;235:602–11.
[43] Xu H, Chen B, Tan P, Cai W, Wu Y, Zhang H, et al. A feasible way to handle the heat management of direct carbon solid oxide fuel cells. Appl Energy 2018;226:881–90.
[44] van Biert L, Woudstra T, Godjevac M, Visser K, Aravind PV. A thermodynamic comparison of solid oxide fuel cell-combined cycles. J Power Sources 2018;397:382–96.
[45] Xu H, Chen B, Tan P, Zhang H, Yuan J, Irvine JTS, et al. Performance improvement of a direct carbon solid oxide fuel cell through integrating an Otto heat engine. Energy Convers Manage 2018;165:761–70.
[46] Buonomano A, Calise F, d'Accadia MD, Palombo A, Vicidomini M. Hybrid solid oxide fuel cells–gas turbine systems for combined heat and power: A review. Appl Energy 2015;156:32–85.
[47] Xu H, Chen B, Zhang H, Tan P, Yang G, Irvine JTS, et al. Experimental and modeling study of high performance direct carbon solid oxide fuel cell with in situ catalytic steam-carbon gasification reaction. J Power Sources 2018;382:135–43.
[48] Xu H, Chen B, Irvine J, Ni M. Modeling of CH_4-assisted SOEC for H_2O/CO_2 co-electrolysis. Int J Hydrogen Energy 2016;41(47):21839–49.
[49] Ni M. 2D thermal modeling of a solid oxide electrolyzer cell (SOEC) for syngas production by H_2O/CO_2 co-electrolysis. Int J Hydrogen Energy 2012;37(8):6389–99.
[50] Tahir M, Amin NS. Photocatalytic CO_2 reduction with H_2O vapors using montmorillonite/TiO_2 supported microchannel monolith photoreactor. Chem Eng J 2013;230:314–27.
[51] Suwanwarangkul R, Croiset E, Fowler MW, Douglas PL, Entchev E, Douglas MA. Performance comparison of Fick's, dusty-gas and Stefan-Maxwell models to predict the concentration overpotential of a SOFC anode. J Power Sources 2003;122(1):9–18.